

# On Some Practical Reactionless Tasks and Energy Consumption Analysis for a Free-Flying Space Manipulator

Hiroki Sone, Dragomir Nenchev<sup>a</sup>

<sup>a</sup>*Department of Mechanical Systems Engineering, Graduate School of Engineering, Tokyo City University, 1-28-1, Tamazutsumi, Setagaya-ku, Tokyo, 158-8557, Japan*

---

## Abstract

This work describes how to use reactionless motion control with a free-floating space robot, suggesting thereby some tasks of practical importance. We show that the reactionless motion capability is directly affected by the kinematic structure of the manipulator, depending thereby upon the existence of kinematic redundancy, a typical lower/upper arm subchain and joint offsets. We investigate a seven-DoF redundant manipulator comprising these features and show that approximate reactionless motions can be obtained with the elbow joint only and/or the wrist joints. Using these reactionless motions, we propose three practical maneuvers for eye-in-hand type inspection, arm deploying/stowing and point-to-point motions with partial reactionless motion. Feasibility is verified via numerical simulations.

*Keywords:* Space robot, Reactionless motion control, Energy consumption

---

## 1. Introduction

Recently, Extra-Vehicular Activity performed by astronauts plays an important role in space development. However, it is known that there are some hazards, such as high vacuum, extreme temperature, cosmic ray and space debris, for human activities in the space environment. Therefore, space robots are expected to perform inspection, construction, assembly and debris removal, instead of astronauts.

In order to realize such missions, the robot controller has to deal with the problem of dynamics coupling between the manipulator and the floating satellite base [1]. It is known that the conventional attitude control system

based on reaction wheels has limited capabilities w.r.t. base attitude disturbances induced by the manipulator motion. To avoid saturation of the reaction wheel signals, the manipulator has to be driven at very low speed. This is not desirable from the perspective of work efficiency and time critical tasks. Therefore, the dynamics coupling and reaction control of the manipulator are as important as its end-effector motion/force control.

As a pioneer work in reaction control, the disturbance map and the enhanced disturbance map was proposed for free-floating manipulator systems [2]. In this method, the base disturbance can be visualized as a color map on the joint space. By using this tool, low reaction path can be eliminated through intuitive manner. However, if the system's degree of freedom (DoF) is more than two, it is difficult to apply this method. 

On the other hand, a path planning method was proposed for zero reaction manipulation. This method is referred to as Reaction Null-Space (RNS) method [3, 4], and provides a straightforward approach to reactionless motion generation. Therein, the condition for reactionless motion is derived from angular momentum conservation law. The method has been confirmed by on-orbit experiments with the Engineering Test Satellite VII (ETS-VII) [5].

In this work, we discuss the following two issues of reactionless motion control: (i) proposal of practical reactionless tasks and (ii) analysis of energy consumption under reactionless motion control. In previous studies, RNS-based reactionless motion controls have been considered. For instance, Dimitrov proposed the angular momentum distribution control for capturing non-cooperative satellite under zero reaction condition [6]. Shah investigated a capability of reactionless motion control with a planar dual-arm system for debris removal [7]. Nguyen proposed adaptive reactionless control considering model uncertainty when capturing an unknown tumbling satellite.

In these studies, it can be seen that position control of the end-effector under reactionless control is assumed. However, it would be impossible in general type of manipulator models due to the limitation of kinematic structure. Indeed, the above methods were verified with two-dimensional models only. The possibility with spatial model is still uncertainty.

For spatial models, some interesting results were reported. With ETS-VII, simple reactionless tasks was proposed for the on-orbit experiment [8][5]. In addition, verification with modified ETS-VII model adding an additional joint was presented. Pisculli proposed the reaction/null Jacobian transpose controller, which is obtained as the filtered version of conventional transpose

Jacobian controller [9]. This method was verified with spatial serial and dual arm manipulator systems with six-DoF manipulators. In that work, it was shown that a reachable region from an initial configuration is quite narrow due to the limitation of the kinematic structure of the model. Nenchev discussed the capability of a singularity treatment method, which is so-called Singularity Consistent Method, to the algorithmic singularity under minimum reaction control problem. It was also confirmed that the workspace of the end-effector becomes quit narrow. In summary, it can be concluded that position control of the end-effector under reactionless control is not feasible in practical tasks even if singularity treatment techniques are used.

The presented author consider that the problem of above studies are arising from the lack of the information of feasible reactionless motion within proposed methods. Hence, in this work, we aim to identify some practical tasks suitable for execution under feasible reactionless motions with typical type of seven-DoF redundant manipulator model. From the empirical analysis, reactionless motion of the applied model can be represented as superposition of the two specific motions: these are the pre-dominant wrist motion and the elbow folding/unfolding motion. Based on the above motions, we identify the following application tasks as prospective from the viewpoint of reactionless motion execution: (i) eye-in-hand inspection, (ii) manipulator reconfiguration, (iii) point-to-point (PTP) transport maneuvers with partial reactionless motion. Among these tasks, only the last one has been considered for reactionless motion control, though with a flexible-base robot [4].

On the other hand, energy consumption has been considered in space systems. In the field of space robot, some reports can be found. Nakamura proposed a control method which reduces energy consumption for free-flying space manipulators with redundant momentum-wheels through kinetic energy conservation [10]. Shah proposed energy optimum reactionless path planning for capturing tumbling satellite [11]. In this method, additional redundancy is used to optimize the kinetic energy of the manipulator. Also



mechanical power was used as a cost function which is to be minimized in [12]. However, it is still uncertainty that energy consumption of reactionless motion compared with the reaction wheel based controllers. In this work, we show that reactionless motion is almost equivalent to the local minimum energy motion under the zero base-attitude deviation. Besides, we show that energy consumption can be reduced through reactionless motion control compared with reaction wheel used controller.

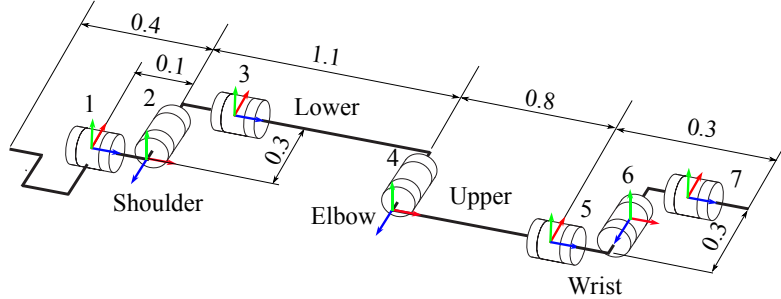


Figure 1: Kinematic structure of the seven-DoF redundant manipulator.

This paper is organized as follows. In the following section we introduce applied model and momentum conservation law as basic notation. Section 3 describes the condition of reactionless control derived from angular momentum conservation law. Besides, we show reactionless motion of the applied model consists of the pre-dominant wrist motion and the elbow folding/unfolding motion. In Section 4, based on these motions, we propose three practical tasks and verify the capability via numerical simulation. Finally, energy consumption of reactionless motion control is discussed in Section 5.

## 2. Basic Notation

In this section, the applied model and basic equation of free-flying space manipulator are presented.

### 2.1. Applied model

In this study, we consider a free-flying space robot model consisting of a satellite base, a serial seven-DoF redundant manipulator and three orthogonal positioned reaction wheels. The manipulator is characterized by a kinematic chain with a distinctive lower/upper arm subchain, including a rotational “elbow” joint and “shoulder” and “wrist” joints with offsets, as shown in Fig. 1. The satellite dimensions and manipulator attachment position are similar to these of ETS-VII, see Fig. 2. The dynamics parameters are shown in Tab. 1. The reaction wheels are modeled as 10 kg mass and  $0.11 \text{ kgm}^2$  moment of inertia.

### 2.2. Momentum Conservation Law

In space environment, it is known that linear and angular momenta are conserved when there is no external force. Actually, the gravity gradient

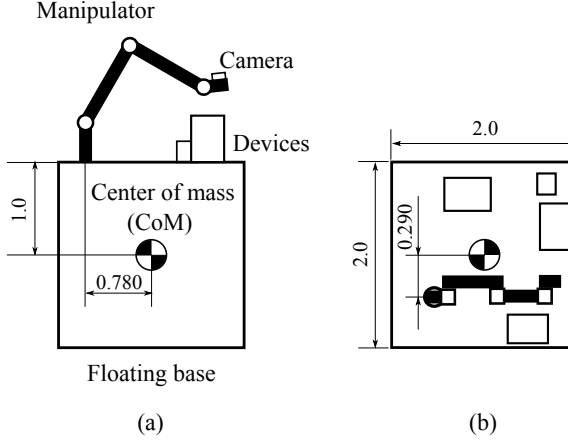


Figure 2: The seven-DoF manipulator attached to the satellite base: (a) side view and (b) top view. Attachment position and dimensions are based on the ETS-VII design [13].

Table 1: Dynamic model parameters

$i$	Mass [kg]		Inertia moment [ $\text{kgm}^2$ ]		
	$m_i$		$I_{xi}$	$I_{yi}$	$I_{zi}$
1	30.0		0.0671	0.0671	0.0851
2	30.0		0.0843	0.267	0.267
3	45.0		3.81	3.81	0.127
4	40.0		0.113	2.19	2.19
5	20.0		0.213	0.213	0.0250
6	20.0		0.0250	0.0292	0.0292
7	25.0		0.0990	0.0990	0.0313

torque and solar radiation force violate these conservation. However, the duration time of the space robot missions are relatively short, we can assume, hence, that the momenta is conservative.

The conservation law of momenta is expressed as follows:

$$\begin{bmatrix} \mathbf{p} \\ \mathbf{l}_b \end{bmatrix} = \begin{bmatrix} \mathbf{M}_v & \mathbf{M}_{v\omega} \\ \mathbf{M}_{v\omega} & \mathbf{M}_\omega \end{bmatrix} \begin{bmatrix} \mathbf{v}_b \\ \boldsymbol{\omega}_b \end{bmatrix} + \begin{bmatrix} \mathbf{M}_{vm} \\ \mathbf{M}_{\omega m} \end{bmatrix} \dot{\boldsymbol{\theta}} + \begin{bmatrix} \mathbf{M}_{vr} \\ \mathbf{M}_{\omega r} \end{bmatrix} \dot{\boldsymbol{\phi}} \quad (1)$$

where,  $\mathbf{p}, \mathbf{l}_b \in \mathbb{R}^3$  denote linear and angular momentum w.r.t. the center of mass (CoM) of the base,  $\mathbf{v}_b, \boldsymbol{\omega}_b \in \mathbb{R}^3$  stand for linear and angular velocity of the base, and  $\dot{\boldsymbol{\theta}} \in \mathbb{R}^7$  and  $\dot{\boldsymbol{\phi}} \in \mathbb{R}^3$  are the joint velocity and the reaction wheel velocity vector, respectively.  $\mathbf{M}_v, \mathbf{M}_{v\omega}, \mathbf{M}_\omega \in \mathbb{R}^{3 \times 3}$  are submatrices

of the composite-rigid-body (CRB) inertia matrix,  $\mathbf{M}_{vm}$ ,  $\mathbf{M}_{\omega r} \in \mathbb{R}^{3 \times 7}$  denote inertia submatrices related to the dynamics coupling between the base and the manipulator.  $\mathbf{M}_{vr}$ ,  $\mathbf{M}_{\omega r} \in \mathbb{R}^{3 \times 3}$  denote inertia matrices related to the dynamics coupling between the base and the reaction wheels. Note that  $\mathbf{M}_{vm}$  and  $\mathbf{M}_{\omega m}$  are referred to as the *coupling inertia matrix*.

For free-flying space manipulators, angular momentum conservation law, especially, is of primary importance. Indeed, it has been noted that even slight variations of the base attitude may cause a failure in the communication between the robot and the ground control center. Angular momentum conservation law can be written in the following form [6]:

$$\mathbf{l}_b = \tilde{\mathbf{M}}_\omega \boldsymbol{\omega}_b + \tilde{\mathbf{M}}_{\omega m} \dot{\boldsymbol{\theta}} + \tilde{\mathbf{M}}_{\omega r} \dot{\boldsymbol{\phi}} \quad (2)$$

where,  $\tilde{\mathbf{M}}_\omega = \mathbf{M}_\omega - \mathbf{M}_{v\omega}^T \mathbf{M}_v^{-1} \mathbf{M}_{v\omega}$ ,  $\tilde{\mathbf{M}}_{\omega m} = \mathbf{M}_{\omega m} - \mathbf{M}_{v\omega}^T \mathbf{M}_v^{-1} \mathbf{M}_{vm}$  and  $\tilde{\mathbf{M}}_{\omega r} = \mathbf{M}_{\omega r}$ . The notation  $(\circ)$  represents a quantity that includes base linear motion effect. In the above equation, the first term on the r.h.s. is the partial angular momentum stemming from base rotation, the second term, on the other hand, results from manipulator motion; it represents the base disturbance in terms of velocity. The term is referred to as the *coupling angular momentum*. Finally, the third term represents the angular momentum stored in the reaction wheels. We consider, momentarily, the system is at free-floating mode ( $\dot{\boldsymbol{\phi}} = \mathbf{0}$ ) until Section 5. For simplify, zero initial momenta are assumed without losing generality, hereafter.

### 3. Reactionless Motion Control: Reaction Null-Space

#### 3.1. Angular momentum-based derivation

Reactionless motions are variations of the manipulator configuration that conserve a zero initial base angular momentum throughout the entire motion. This implies  $\boldsymbol{\omega}_b = \mathbf{0}$ , and hence,

$$\tilde{\mathbf{M}}_{\omega m} \dot{\boldsymbol{\theta}} = \mathbf{0}. \quad (3)$$

From this equation, the set of reactionless motion can be represented as [14]:

$$\dot{\boldsymbol{\theta}} = \mathbf{P}_{RNS} \dot{\boldsymbol{\theta}}_a, \quad (4)$$

where,  $\mathbf{P}_{RNS} (= \mathbf{E} - \tilde{\mathbf{M}}_{\omega m}^+ \tilde{\mathbf{M}}_{\omega m}) \in \mathbb{R}^{7 \times 7}$  denotes a projector onto the null-space of the coupling inertia matrix,  $\mathbf{E} \in \mathbb{R}^{7 \times 7}$  is the identity matrix and

$(\circ)^+$  stands for the pseudoinverse matrix.  $\dot{\theta}_a \in \mathbb{R}^7$  is an arbitrary vector with the dimensions of joint velocity. It plays the role of a vector-parameter for the set of reactionless motions. It is apparent that the null-space of the coupling inertia matrix, referred henceforth as the *Reaction Null-Space* (RNS), plays an important role for reactionless motion generation. Here, it should be noted that all of reactionless motions can be represented in the above notation. Hence, the zero reaction motions generated by other methods, e.g. nonlinear optimization programming and so on, are basically same as that of (4).

### 3.2. Analysis of reactionless motion with the applied model

Before proceeding with the proposal of practical reactionless motion tasks, we have to identify reactionless motion with our manipulator model. In this model, the DoF of reactionless motion is four, which is obtained as the difference between the joint number and the base attitude DoF (three). The following discussion provides a useful representation of the four-DoF motion.

At first, we divide the kinematic structure into positioning and wrist subchains for practical aspect. The positioning subchain (PS) consists of Joint 1 through 4. The rest of joints constitute the wrist subchain (WS).

Here, we focus on the amplitude of the angular momentum produced by each subchain. Because of the small mass and length of the momentum arm, we can regard that the angular momentum under WS motion is far smaller than that of PS. Hence, it can be considered that PS can compensate the disturbance induced by WS motion, completely. In other words, a part of the reactionless motion consists of free WS motion and small PS motion as shown in Fig. 3 (a). This motion is three-DoF reactionless motion and is defined as the pre-dominant wrist motion, hereafter.

The remaining one-DoF reactionless motion is uniquely determined as the null-space of the submatrix of the coupling inertia matrix related to the PS part. This motion approximately consists of the elbow folding/unfolding motion as shown in Fig. 3 (b). From angular momentum conservation, we can assume that the motion of Joint 1 and 2 are relatively small in the above two motions.

These motions are represented as follows:

$$\dot{\theta} = \begin{bmatrix} \mathbf{B}(\theta) \\ \mathbf{E}_{3 \times 3} \end{bmatrix} \dot{\theta}_W + b \begin{bmatrix} \mathbf{n}(\theta) \\ \mathbf{0}_3 \end{bmatrix} \quad (5)$$

$$\mathbf{B}(\theta) = -\tilde{\mathbf{M}}_{\omega m, P}^+ \tilde{\mathbf{M}}_{\omega m, W} \quad (6)$$

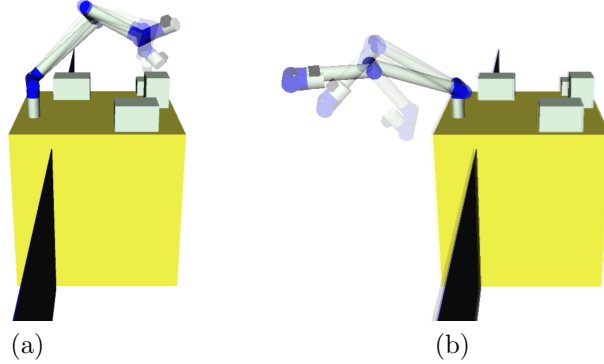


Figure 3: Reactionless motion of the applied model: (a) pre-dominant wrist motion and (b) elbow folding motion.

where,  $\dot{\boldsymbol{\theta}}_W \in \mathbb{R}^3$  stands for the joint velocity of WS,  $\mathbf{B}(\boldsymbol{\theta}) \in \mathbb{R}^{4 \times 3}$  is a linear map from the WS's disturbance to the joint velocity of PS.  $\tilde{\mathbf{M}}_{\omega m,P} \in \mathbb{R}^{3 \times 4}$ ,  $\tilde{\mathbf{M}}_{\omega m,W} \in \mathbb{R}^{3 \times 4}$  are submatrices of the coupling inertia matrix related to PS and WS,  $\mathbf{n} \in \mathbb{R}^4$  is a null-space vector of  $\tilde{\mathbf{M}}_{\omega m,P}$ . This vector can be obtained as co-factor of  $\tilde{\mathbf{M}}_{\omega m,P}$ .  $b$  is an arbitrary scalar,  $\mathbf{E}_{3 \times 3} \in \mathbb{R}^{3 \times 3}$  and  $\mathbf{0}_3 \in \mathbb{R}^3$  denote the identity matrix and zero matrix, respectively.

In the above equation, the first term on the r.h.s. represents the pre-dominant wrist motion; the second term represents the approximate elbow folding/unfolding motion. It should be noted that these motions have orthogonal property because of  $\mathbf{B}^T \mathbf{n} = \mathbf{0}$ . Hence it is apparent that reactionless motion of the model is represented as superposition of these motions.

From the above analysis, we can obtain the following fact: because the end-effector position largely depends on the motion of PS, the DoF of the end-effector position control is approximately 1 according to that of PS. Namely, even if the system has enough DoF, position control under reactionless motion is not feasible due to the limitation of the kinematic structure with general type of manipulators. This is the reason why almost all previous methods, which assume the position control of the end-effector, are not applicable. Hence, we have to consider feasible reactionless motion when applying reactionless control for practical tasks.

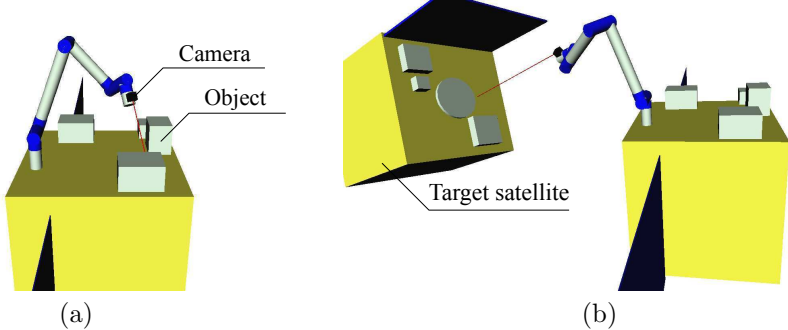


Figure 4: Inspection maneuver using the hand camera: (a) inspection for own-satellite attached devices and (b) refueled satellites observation.

#### 4. Proposal and verification of reactionless motion tasks

In this section, we propose three practical task candidates to be executed under reactionless motion, as specified in the previous section. The first candidate is an inspection task using the end-effector hand camera. The second one is a manipulator reconfiguration maneuver: especially, manipulator deployment/stowing maneuver is assumed. The third one is a general PTP motion tasks.

##### 4.1. Inspection with the hand camera

One frequent tasks for free-floating space robots is inspection of various devices mounted on satellites, large space structures or serviced satellites, with a camera attached to the end-effector as shown in Fig. 4. Such task was also performed within the ETS-VII mission [15]. Once the arm is positioned appropriately, the camera view angle for inspection is changed by rotating the wrist. This task is a good candidate for a reactionless maneuver since the hand camera is assumed to be lightweight.

we consider following three conditions in order to realize inspection.

1. Orientation control of the end-effector (three-DoF)
2. Reactionless constraint (three-DoF)
3. Stabilization of the wrist position

The third one is due to the following reason: the large displacement deflection of the wrist might induce collision problem and camera view change.

The control command of the joint velocity, considering the above three conditions, can be obtained as follows:

$$\dot{\boldsymbol{\theta}}^{ref} = \mathbf{G}_\omega^+ \begin{bmatrix} \mathbf{0} \\ \boldsymbol{\omega}_e^{ref} \end{bmatrix} + k_g \mathbf{P}_{G_\omega} [\mathbf{A} \mathbf{J}_{Wv}]^T \Delta \mathbf{x}_W \quad (7)$$

where,  $\mathbf{G}_\omega = [\tilde{\mathbf{M}}_{\omega m}^T \ \mathbf{J}_\omega^T]^T \in \mathbb{R}^{6 \times 7}$  is a constraint matrix,  $\mathbf{P}_{G_\omega} \in \mathbb{R}^{7 \times 7}$  is a projector onto the null-space of  $\mathbf{G}_\omega$ ,  $\mathbf{J}_\omega \in \mathbb{R}^{3 \times 7}$  and  $\mathbf{J}_{Wv} \in \mathbb{R}^{3 \times 7}$  stand for the Jacobian w.r.t. the angular velocity of the end-effector and wrist linear velocity, respectively.  $\Delta \mathbf{x}_W \in \mathbb{R}^3$  is the wrist-position deflection from the initial one,  $k_g$  is a scalar gain.

The first term is used to perform reactionless orientation control of the wrist, and the second term is the gradient vector of the following potential function:

$$V = \frac{1}{2} \Delta \mathbf{x}_W^T \mathbf{A} \Delta \mathbf{x}_W \quad (8)$$

where,  $\mathbf{A}$  is a weight matrix.

Note that the frequency of arriving at algorithmic singularity with this formulation is approximately the same as the occurrence of wrist kinematic singularities. Nevertheless, it is advisable to employ singularity treatment techniques, such as the Singularity-Consistent method [16] for example. Also, care should be taken to avoid stationary-point type local minima of the null-space gradient optimization.

In what follows, we examine the performance under (7) by comparing to the conventional inverse kinematic controller via numerical simulations. We assume the task of inspecting a target satellite before refueling like mission, as shown in Fig. 4 (b). The initial configuration is set as  $[90 \ -30 \ 0 \ -70 \ 180 \ -30 \ 0]^T$  deg the reference angular velocity is  $\boldsymbol{\omega}_e^{ref} = \pi[s(t) \ 0 \ 0]^T$ , where  $0 \leq s(t) \leq 1$  denotes a fifth-order polynomial interpolation. The simulation results are displayed in Fig. 5 and Fig. 6. These are obtained with  $k_g = 100$ , the weight matrix set as the identity matrix. From the results in Fig. 5 (a) it is seen that, with the proposed method, the rotation of the end-effector can be accomplished without inducing reactions to the base. In contrast, a relatively large base orientation change can be observed under the conventional control method, despite the low inertia parameters of the wrist (see Fig. 5 (b)). From the wrist deflection graph in Fig. 6 it becomes apparent that the effect of the cost function leads to a sufficiently

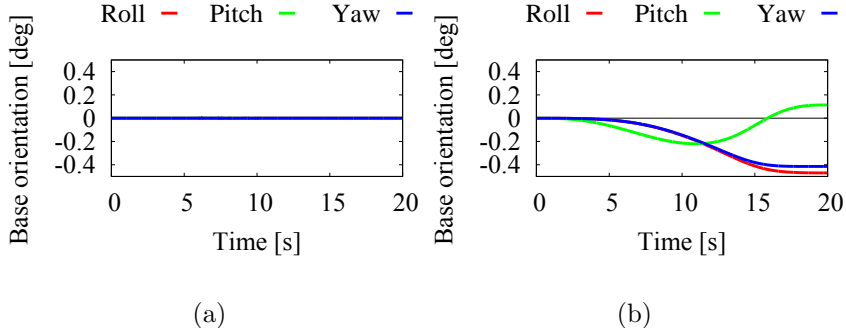


Figure 5: Comparison results of inspection maneuver: (a) reactionless motion control and (b) inverse Jacobian controller.

small deviation from the initial wrist position. Hence, we can conclude that this motion maneuver is applicable as an inspection maneuver using the hand camera.

#### 4.2. PTP positioning maneuver with partial reactionless motion

PTP motion maneuvers are widely used. Due to the reasons outlined above, we restrict our attention to a specific subset of PTP maneuvers: arm reconfiguration tasks wherein the hand does not hold an object. It would be desirable to execute such maneuvers under reactionless motion control. This, however, is impossible for arbitrary points since reactionless motions are quite restricted, as already explained. Nevertheless, reactionless motion can be useful, if the PTP motion is planned appropriately. One possibility is to combine a reactionless motion with a conventional PTP motion. This method was originally proposed in [17]; it has been referred to as the *3-phase method* and applied to a planar flexible-base robot [18]. From this study, it became apparent that the method can be used for motions with large displacements. The method has not been verified for the case of a free-floating robot. Below we show how to adopt the 3-phase method to PTP motion with our spatial free-floating model. Before doing so, we will review the 3-phase method briefly.

##### 4.2.1. 3-phase method

The joint path that connects the specific initial and final configurations is designed by connecting three sub-paths. In Fig. 7, Phases I and III are reactionless paths. Phase II is a conventional (non-reactionless) PTP path used to connect the two reactionless motion paths. The primary concern is

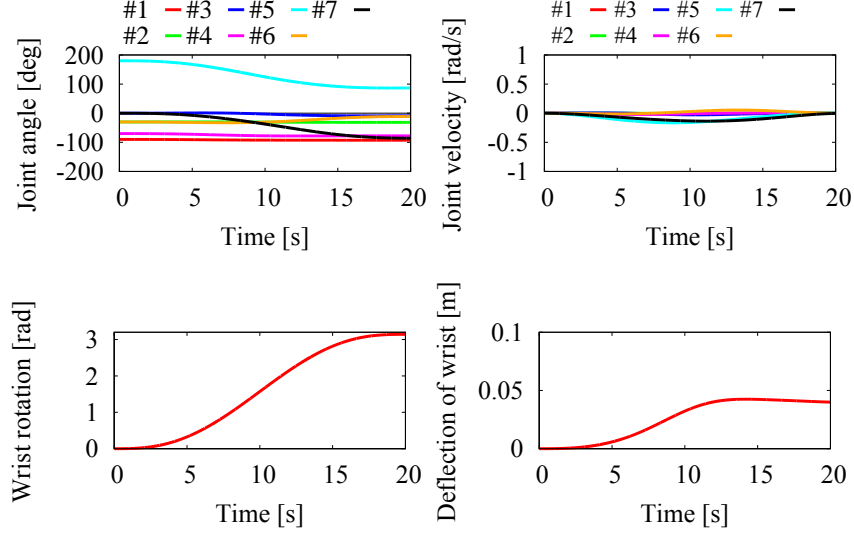


Figure 6: Camera inspection maneuver with reactionless end-tip orientation control. The deflection of the wrist position from the initial one can be made sufficiently small via the gradient gain  $k_g$ .

how to determine the three sub-paths to obtain the smallest possible base reaction during the PTP sub-path (Phase II). In [18], a folded-arm configuration is used for Phase II as this configuration induces small reaction due to the property of the flexible-base model.

In general, it is desirable to obtain the optimal path for reaction minimization during the second phase (Phase II). However, because of the high dimension and the non-linearity of the system, it is difficult to obtain the optimal solution. Therefore, we adopt here the folded-arm configuration as a suitable configuration during the second phase. Recall that the folding/unfolding of the arm can be always done along reactionless paths. We provide a theoretical argument of reaction reduction with the folded configuration in what follows.

The coupling angular momentum can be rewritten in the following form:

$$\tilde{\mathbf{M}}_{\omega m} \dot{\boldsymbol{\theta}} = \left\{ \sum_{i=1}^7 \mathbf{I}_i \mathbf{J}_{\omega i} \right\} \dot{\boldsymbol{\theta}} + \left\{ \sum_{i=1}^7 m_i [\mathbf{r}_i^\times] \mathbf{J}_{vi} \right\} \dot{\boldsymbol{\theta}} - \left\{ m_C [\mathbf{r}_C^\times] \mathbf{J}_C \right\} \dot{\boldsymbol{\theta}}, \quad (9)$$

where  $\mathbf{I}_i \in \mathbb{R}^{3 \times 3}$  is the link inertia tensor,  $\mathbf{J}_{vi}, \mathbf{J}_{\omega i} \in \mathbb{R}^{3 \times n}$  are the Jacobian

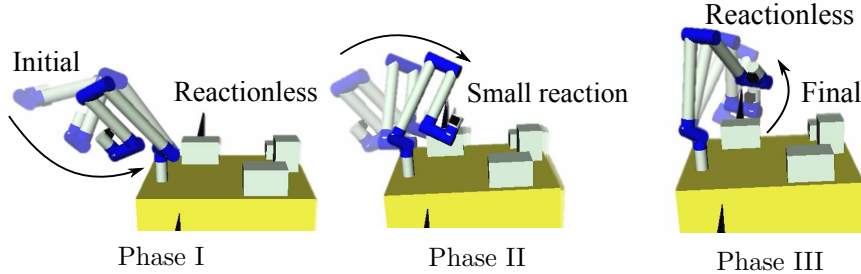


Figure 7: 3-phase method: PTP maneuver with partial reactionless paths.

matrices w.r.t. the linear and angular velocity of each link,  $\mathbf{r}_i$  and  $\mathbf{r}_C \in \mathbb{R}^3$  are position vectors of the CoM of each link and the whole system w.r.t. base frame,  $m_i$  and  $m_C$  denote masses of each link and the whole system, respectively.  $(\circ)^\times$  stand for a skew-symmetric matrix for the respective vector.

It is apparent that the coupling angular momentum consists of two components. The first one is the angular momentum stemming from the rotational motion of each link, i.e. the first term on the r.h.s. of (9). The second one is the angular momentum due to the translational motion of the CoM of each link, i.e. the second and third terms. These two components are smallest when the manipulator is folded, for the following reasons. First, in the case of rotational motion, the inertia tensor of the manipulator is smallest when the manipulator is folded. Hence, the rotational reaction can be reduced. Next, from the second and third term in (9) it is seen that the translational reaction is related to the CoM position of each link. In the folded configuration, the manipulator CoM is closest to the CoM of the base and the linear velocity becomes small. As a result, the translational reaction can be also reduced. For these reasons, in this work we use the folded configuration during Phase II.

#### 4.2.2. Verification via simulations

We verified the control performance of partial reactionless motion planning via numerical simulations in comparison to conventional control methods. The initial configuration is  $[-20 - 40 0 - 60 180 180 0]^T$  deg, the final one is  $[-120 50 0 - 60 180 180 0]^T$  deg, or  $[-1.7 0.45 1.7]^T$  m for task-space controllers in comparison. These two configurations cannot be linked via a reactionless path. Therefore, we apply the 3-phase method. Phase I is a reactionless motion path from the initial configuration toward folded arm configuration FA-1. Phase III is determined from a reversed reactionless

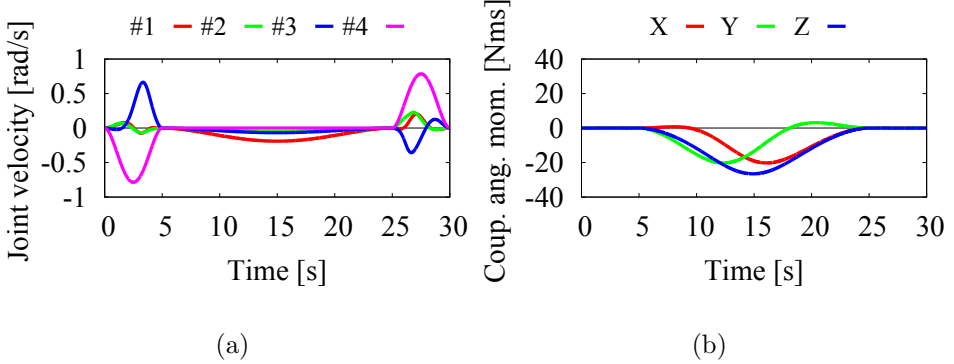


Figure 8: Simulation results of 3-phase method: (a) joint velocity and (b) coupling angular momentum.

motion starting from the final configuration toward folded-arm configuration FA-2. These reactionless motions are obtained from the second term on the r.h.s. in (6).

$$\dot{\boldsymbol{\theta}}^{ref} = \frac{\dot{\theta}_4^{ref}(t)}{n_4} \begin{bmatrix} \mathbf{n} \\ \mathbf{0}_3 \end{bmatrix} \quad (10)$$

$$\dot{\theta}_4^{ref}(t) = \dot{\theta}_4^{des}(t) + k_p \Delta\theta_4(t) \quad (11)$$

where  $n_4$  is the forth element of  $\mathbf{n}$ ,  $\theta_4^{des}$  is the desired trajectory of Joint 4,  $\Delta\theta_4$  is the error between the desired and current one.  $k_p$  is a scalar as the feedback gain. The two folded-arm configurations are distinct and uniquely defined as resultant configurations along the respective reactionless paths, wherein  $\theta_4 = -\pi$  rad. In the simulation, Phase I and III are executed in 5 seconds, and Phase II in 20 seconds. For comparison, three traditional methods were simulated, such as joint space interpolation (JS-C), inverse Jacobian controller (IJ-C) and transpose Jacobian controller (TJ-C) under the same condition. Note that, for the sake of simplicity, orientation of the end-effector is not considered here. Hence, the positioning subchain is only driven.

At first, we show the simulation results of partial reactionless maneuver in Fig. 8. From the results, it can be seen that joint motion seems to be smooth and the coupling angular momentum is only induced in Phase II.

For comparison, we show the base attitude deviation in each method in Fig. 9. It can be seen that 3-phase method can reduce the base attitude deviation compared with the others. Actually, the deviation of the roll axis

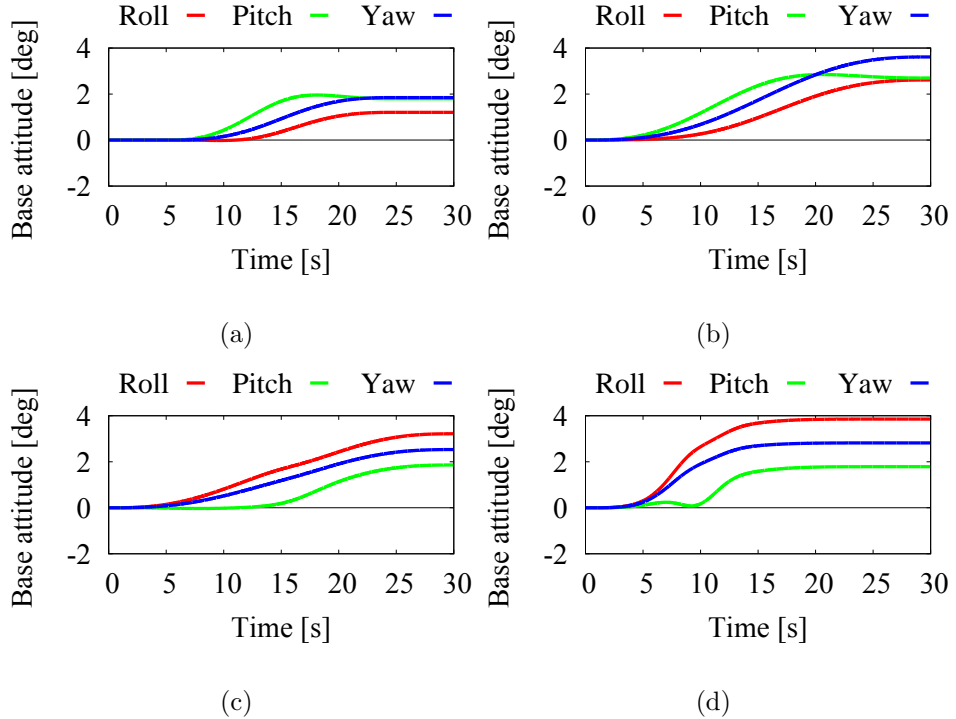


Figure 9: Base attitude deviation: (a) 3-phase method, (b) JS-C, (c) IJ-C and (d) TJ-C. Among these controllers, 3-phase method is the best way from the perspective of reaction reduction.

for the proposed motion is, at least, as half as that of the others. Note that, along the reactionless paths, the joint rates can be scaled so that the maximum joint rate can be reached for certain joints, that would further increase the efficiency. From these results, we can conclude that reactionless motion is useful even if it is used, partially.

#### 4.3. Reconfiguration maneuver from the stowed configuration

Finally, we discuss reconfiguration maneuver from the stowed configuration. When, launching a free-floating space robot into orbit, the manipulator has to be stowed. These configurations are referred to as the *stowed configuration* as shown in the upper left part of Fig. 10. During on-orbit experiments, deployment and stowing of a manipulator is executed multiple times. Hence, this task is a good candidate for reactionless motion control, when aiming at improved mission efficiency. In this work, we introduce partial reactionless deployment maneuver as similar manner to the 3-phase method.

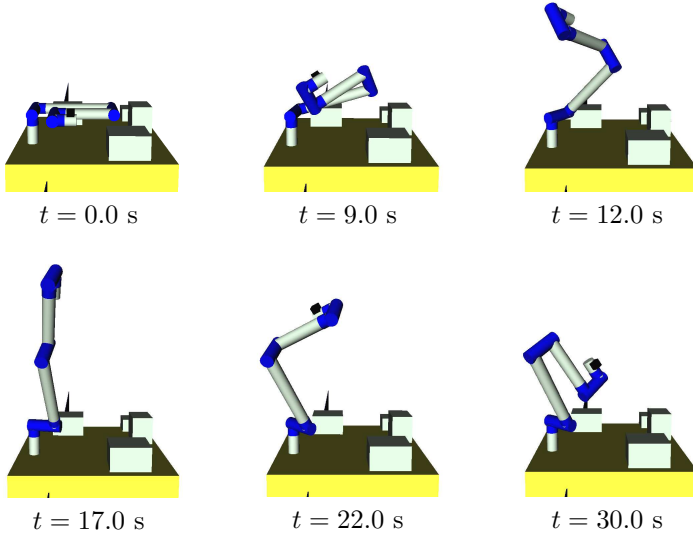


Figure 10: Motion snapshots from the deployment maneuver under reactionless motion control.

#### 4.3.1. Examination of the capability of fully reactionless deployment

At first, we examine reactionless motions from the stowed configurations. Note that, for the sake of simplicity, the positioning subchain is only considered here, because the effect of the wrist motion is relatively small within reconfiguration. Further on, since only the four joints of the positioning subchain are employed, the dimension of the RNS is one. Therefore, the reactionless motion path is uniquely determined by the initial (stowed) configuration. The final (deployed) configuration can be selected as any configuration along the reactionless path. The selection will depend upon the subsequent task. Careful planning for the stowed/deployed configuration is needed. The benefit is that the speed/acceleration along the reactionless path connecting the two configurations can be set freely which allows for a very time-efficient deployment.

We denote the candidates for the stowed configuration of our model as follows:

$$\boldsymbol{\theta}_{st} = \{ \boldsymbol{\theta} \in \mathbb{R}^7 \mid \theta_i = \pm\pi/2, \theta_j = 0, \pm\pi, \forall \theta_6, \forall \theta_7 \} \\ (i = 1, 2, j = 3 \text{ to } 5). \quad (12)$$

We pick up a configuration that is well-conditioned for the reactionless mo-

tion:  $[\pi/2 \ - \pi/2 \ 0 \ - \pi \ \pi, \theta_6, \theta_7]^T$  rad, where  $\theta_6$  and  $\theta_7$  can be arbitrary value. Snapshots from the deployment sequence are shown in Fig. 10, with  $\theta_6 = \pi$ ,  $\theta_7 = 0$  rad. It can be seen that the reactionless motion path is passing through an appropriate point for an inspection maneuver ( $t = 30$  s). Hence, it is possible to execute an inspection maneuver immediately after deployment in this case.

However, it should be noted that this maneuver is only available when a useful reactionless motion path can be prepared for specific tasks. For instance, it is not sure if reactionless reconfiguration for pre-positioning task before refueling mission, as shown in Fig. 4 (b), can be used. From this reason, we introduce more feasible reconfiguration maneuver through sacrificing fully reactionless property.

#### *4.3.2. Partial reactionless deployment maneuver*

Here, we present a reconfiguration maneuver for the purpose of the base reaction reduction. We use a specific part of the 3-phase method, especially Phase II and III, because the elbow joint is folded at the stowed configuration. Hence, the same approach as 3-phase method can be used, straightforwardly. From the result of PTP maneuver, the base deviation under the partial reactionless reconfiguration would be, at least, smaller than conventional methods.

We demonstrate the pre-positioning task for observation of refueled satellites as explained above (Fig. 4 (b)). The initial configuration is set as the same stowed configuration as explained above. The final configuration is set as  $[90 \ 50 \ 0 \ -300 \ 0 \ 20 \ 0]^T$  deg. The middle point configuration, which two motions are switched at, is obtained as the terminal configuration from the final to the elbow folded configuration  $\theta_4 = \pi$  rad.

Snapshot of the motion maneuver is displayed in Fig. 11. For comparison, joint space interpolation with straight line trajectory is performed in the same condition as shown in Fig. 12. The final (and also maximum) base-attitude deviation under the proposed method is 5.48 deg at pitch direction. In the case of the joint space interpolation, 7.66 deg attitude deviation is observed at the same direction. As a result, it can be realized 28.5% reduction of the base-attitude deviation.

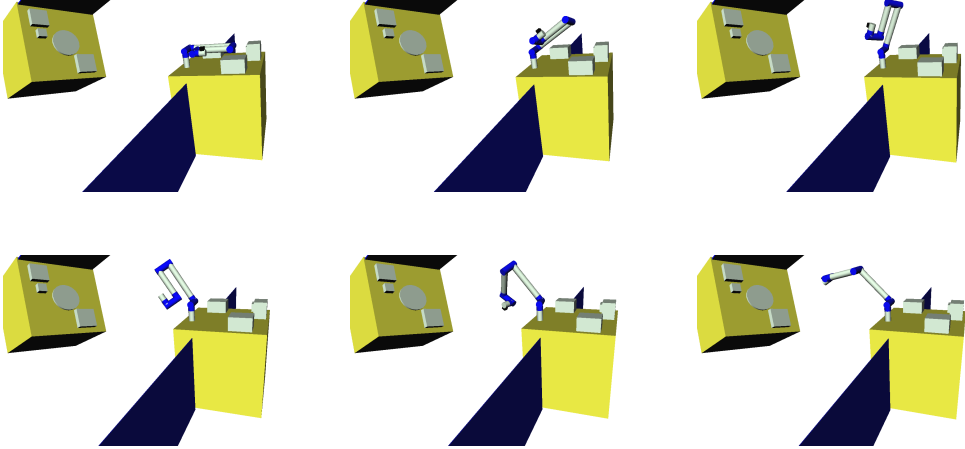


Figure 11: Proposed reconfiguration maneuver using reactionless motion partially.

## 5. Energy consumption analysis under zero base-attitude deviation

Here, we identify energy consumption under zero base-attitude deviation ( $\omega_b \approx \mathbf{0}$ ). We restrict our attention to the system which consists of one manipulator and three reaction wheels. Because of no usage of reaction wheels, reactionless motion control would be a better way in terms of energy consumption. Actually, reactionless motion is almost equivalent as the local minimum energy motion under zero-attitude deviation. We show this results through numerical analysis in this section.

### 5.1. Kinetic energy representation in terms of the joint velocity

In this work, we assume that kinetic energy is used to evaluate energy consumption. For simplify, we ignore energy losses arising from friction, heat and electric part. The kinetic energy of the space robot system can be written as [1]:

$$T = \frac{1}{2} \omega_b^T \tilde{\mathbf{M}}_\omega \omega_b + \omega_b^T [\tilde{\mathbf{M}}_{\omega m} \quad \tilde{\mathbf{M}}_{\omega r}] \begin{bmatrix} \dot{\theta} \\ \dot{\phi} \end{bmatrix} + \frac{1}{2} [\dot{\theta}^T \quad \dot{\phi}^T] \begin{bmatrix} \tilde{\mathbf{M}}_m & \mathbf{0} \\ \mathbf{0} & \tilde{\mathbf{M}}_r \end{bmatrix} \begin{bmatrix} \dot{\theta} \\ \dot{\phi} \end{bmatrix} \quad (13)$$

where, the first term on the r.h.s. represents the partial kinetic energy stemming from base rotation, the second term is coupling kinetic energy between the base and the manipulator or the reaction wheels. Finally, the third term is the partial kinetic energy produced by the manipulator and the reaction wheels.

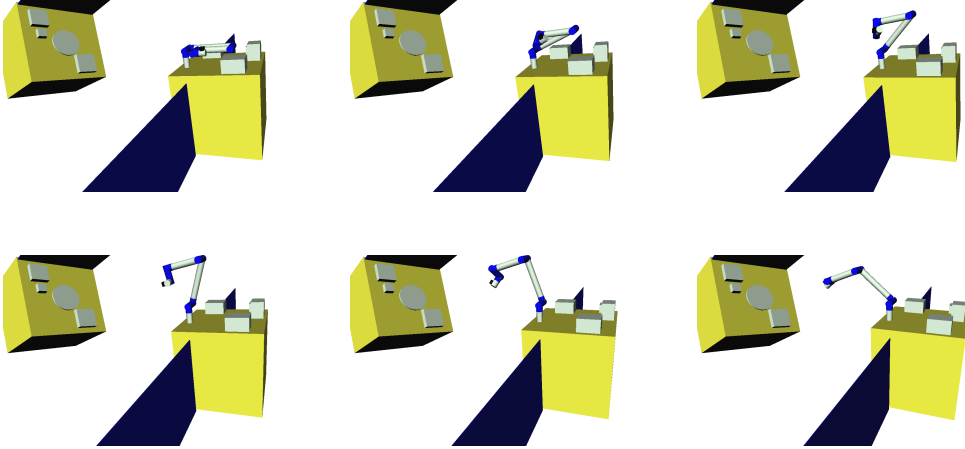


Figure 12: Reconfiguration maneuver through the joint space interpolation with straight line trajectory.

With the assumption  $\omega_b \approx \mathbf{0}$ , (13) can be simplified as:

$$T = \frac{1}{2} \dot{\theta}^T \tilde{M}_m \dot{\theta} + \frac{1}{2} \dot{\phi}^T \tilde{M}_r \dot{\phi} \quad (14)$$

In addition, from angular momentum conservation, the reaction wheel speed can be represented as a function of the joint velocity,  $\dot{\phi} = -\tilde{M}_{\omega r}^{-1} \tilde{M}_{\omega m} \dot{\theta}$ . By substituting the above equation into (14), we can obtain the kinetic energy as a function of the joint velocity as follows:

$$\begin{aligned} T &= \frac{1}{2} \dot{\theta}^T \left( \tilde{M}_m + \tilde{M}_{\omega m}^T (\tilde{M}_{\omega r} \tilde{M}_r^{-1} \tilde{M}_{\omega r}^T)^{-1} \tilde{M}_{\omega m} \right) \dot{\theta} \\ &= \frac{1}{2} \dot{\theta}^T \left( \tilde{M}_m + I_r^{-1} \tilde{M}_{\omega m}^T \tilde{M}_{\omega m} \right) \dot{\theta} \\ &= \frac{1}{2} \dot{\theta}^T (\Lambda_m + \Lambda_r) \dot{\theta} \end{aligned} \quad (15)$$

where,  $\Lambda_m = \tilde{M}_m$ ,  $\Lambda_r = I_r^{-1} \tilde{M}_{\omega m}^T \tilde{M}_{\omega m} \in \mathbb{R}^{n \times n}$  are the inertia matrix of the manipulator and the reaction wheels under zero attitude deviation. These matrices represent the feature of the kinetic energy w.r.t. the joint motion. Note that  $\tilde{M}_{\omega r} \approx \tilde{M}_r$  and  $\tilde{M}_r = \text{diag}(I_r, I_r, I_r)$  are used. Besides, we assume that the reaction wheels are arranged on each orthogonal axis on the base coordinate according to zero-momentum stabilization, and these inertia moments are same.

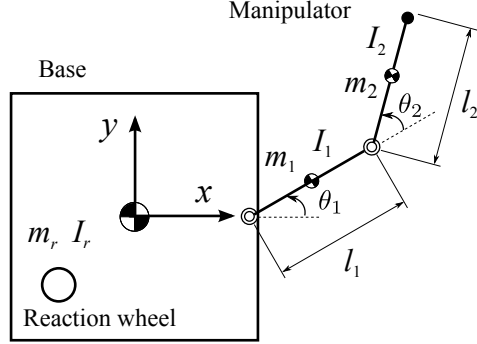


Figure 13: The link length, mass, inertia moment are set to  $l_i = 1$  m,  $m_i = 100$  kg,  $I_i = 8.3$  kgm $^2$  ( $i = 1, 2$ ), respectively. The reaction wheel mass and inertia moment are set to  $m_r = 10$  kg,  $I_r = 0.11$  kgm $^2$ . Note that kinetic energy for reaction compensation does not depend on the base parameters.

### 5.2. Local minimum energy motion under zero base-attitude deviation

(15) represents kinetic energy under zero base-attitude deviation. With using the same way as the coupling map [19], the local minimum energy motion can be obtained through Singular-Value-Decomposition (SVD) of the inertia matrix  $\Lambda = \Lambda_m + \Lambda_r$ :

$$\Lambda = \sigma_1 \mathbf{u}_1 \mathbf{v}_1^T + \sigma_2 \mathbf{u}_2 \mathbf{v}_2^T + \cdots + \sigma_n \mathbf{u}_n \mathbf{v}_n^T \quad (16)$$

where,  $\sigma_i$  is singular value,  $\mathbf{u}_i$  and  $\mathbf{v}_i$  are the left and right singular vector. In this equation, physically,  $\mathbf{v}_i$  stands for the normalized joint velocity and  $\sigma_i$  represents kinetic energy induced by the joint motion  $\mathbf{v}_i$ . Since the property of SVD,  $\sigma_n$  represents minimum kinetic energy, instantaneously. Hence,  $\mathbf{v}_n^T$  represents the local minimum energy motion.

### 5.3. Numerical verification

Here, we compare reactionless motion and the local minimum energy motion via numerical analysis. For simplify, we focus on models which have one-DoF reactionless motion, only.

#### 5.3.1. Case 1: two-DoF planar manipulator

At first, two-DoF planar model is considered, which is shown in Fig. 13. The link length, mass and inertia moment are set to  $l_i = 1.0$  m,  $m_i = 100$  kg and  $I_i = 8.3$  kgm $^2$  ( $i = 1, 2$ ), respectively. The reaction wheel's mass and inertia moment are set to  $m_r = 10$  kg,  $I_r = 0.11$  kgm $^2$ . Note that kinetic

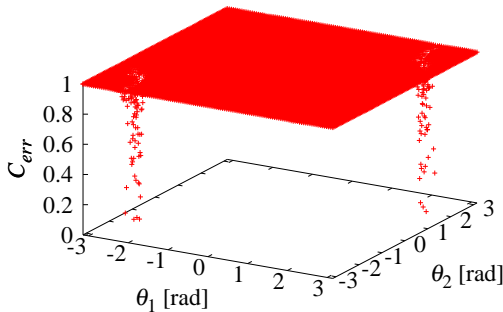


Figure 14: The distribution of the cost function with two-DoF model.

energy for reaction compensation does not depend on the base parameters. Hence, any values can be considered.

Here, we consider the following cost function to evaluate equivalence between reactionless motion and local minimum energy motion:

$$C_{err} = |\dot{\theta}_{min}^T \dot{\theta}_{rlm}| \quad (17)$$

where,  $\dot{\theta}_{min}, \dot{\theta}_{rlm} \in \mathbb{R}^n$  denote the local minimum energy motion and reactionless motion, respectively. Note that these vectors are normalized.

This cost function represents the direction cosine between these vectors. Hence, taking  $C_{err}$  closed to 1 implies these motions are equivalent. This function will be calculated at 10000 points in the joint space with  $-\pi \leq \theta_i \leq \pi$ , ( $i = 1, 2$ ). For each coordinate, joint angle are discretized with  $\Delta\theta_i = 6.28 \times 10^{-2}$  rad.

According to (16),  $\dot{\theta}_{min}$  can be obtained as  $\mathbf{v}_2$  and reactionless motion is obtained through SVD of the coupling inertia matrix. The distribution of  $C_{err}$  is displayed in Fig. 14. From the result, we can confirm that  $C_{err} \approx 1$  at almost all points. Actually, average of  $C_{err}$  is 0.9996 among all points. Hence, these motions are equivalent in this model. Here, we should note that there is large error in two specific points; these points are related to the singularity of the coupling inertia matrix. More depthful discussion will be done with spatial model in Section 5.4

Before discussing spatial model, we should identify an influence arising from parameter variation. Here, we focus on total link mass and length

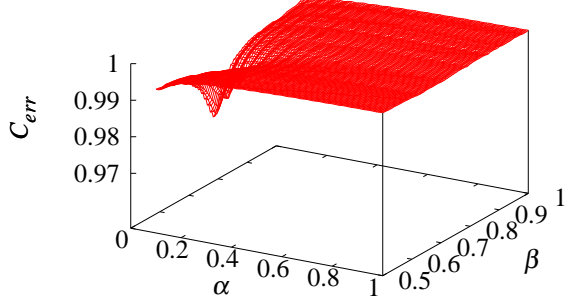


Figure 15: This figure shows that how the average of  $C_{err}$  is effected from parameter variation.

according to the following equation:

$$m_i^* = \alpha m_i \quad (18)$$

$$l_i^* = \beta l_i \quad (19)$$

where,  $0.1 \leq \alpha \leq 1$ ,  $0.5 \leq \beta \leq 1$  are scaling factor,  $m_i$ ,  $l_i$  are the original mass and length as explained above ( $m_i = 100$  kg,  $l_i = 1$  m).  $(\circ)^*$  denotes the modified parameter. Average of  $C_{err}$  under the parameter variation is displayed in Fig. 15. This figure shows that reactionless motion coincides local minimum motion even if parameters are changed. Especially, high equivalence can be observed when  $\alpha$  is closed to 1, namely the link mass is larger.

### 5.3.2. Case 2: four-DoF spatial manipulator

Here, we identify the equivalence with a four-DoF spatial manipulator. As the applied model, the positioning subchain of the seven-DoF redundant manipulator is considered. In this case, the same cost function is also used to evaluate equivalence. The calculation range is follows:

$$\begin{aligned} -\pi &\leq \theta_i \leq \pi \\ \Delta\theta_i &= 0.125 \text{ rad } (i = 1, 3, 4) \end{aligned} \quad (20)$$

$$\begin{aligned} -\frac{\pi}{2} &\leq \theta_2 \leq \frac{\pi}{2} \\ \Delta\theta_2 &= 0.0628 \text{ rad} \end{aligned} \quad (21)$$

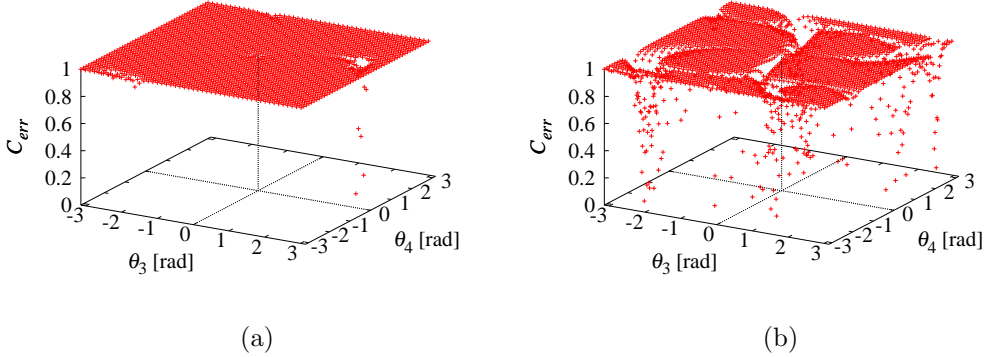


Figure 16: The distribution of cost function in four-DoF spatial manipulator model: (a) regularly appearing distribution  $(\theta_1, \theta_2) = (0, 0.785)$  rad and (b) special case  $(\theta_1, \theta_2) = (0.523, 0)$  rad.

where, we restrict the range of joint 2 because almost all configurations over the above range have no meaning due to the collision with the satellite. Totally, the cost function is calculated at  $6.25 \times 10^6$  points.

Because of too many parameters to draw graph, we show that the distribution of  $C_{err}$  parametrized for joint 1 and 2. Among almost all results, the graphs can be divided into two type of distribution as displayed in Fig. 16.

Regularly appearing case is shown in Fig. 16 (a). This map shows that there is no large error in almost all configurations. On the other hand, relative large error is, hardly never, appeared as shown in Fig. 16 (b). Despite these errors, the average values of  $C_{err}$  in all configurations can be obtained as 0.995. Hence, reactionless motion is also equivalent to local minimum energy motion in this spatial model.

#### 5.4. Discussion

Here, we discuss why these motions are equivalent. To answer the above question, we should identify a property of kinetic energy produced by the manipulator and the reaction wheels under the zero base-attitude condition. This property is appeared in the inertia matrix.  $\Lambda_m$  and  $\Lambda_r$  are rewritten in

the following form:

$$\boldsymbol{\Lambda}_m = \sum_{i=1}^n \left\{ m_i \mathbf{J}_{vi}^T \mathbf{J}_{vi} + \mathbf{J}_{\omega i}^T \mathbf{I}_i \mathbf{J}_{\omega i} \right\} \quad (22)$$

$$\begin{aligned} \boldsymbol{\Lambda}_r = & \frac{1}{I_r} \sum_{i=1}^n \left\{ m_i^2 \mathbf{J}_{vi}^T [\mathbf{r}_i \times]^T [\mathbf{r}_i \times] \mathbf{J}_{vi} + \mathbf{J}_{\omega i}^T \mathbf{I}_i \mathbf{I}_i \mathbf{J}_{\omega i} + \right. \\ & \left. m_i \mathbf{J}_{\omega i}^T \mathbf{I}_i [\mathbf{r}_i \times] \mathbf{J}_{vi} + [m_i \mathbf{J}_{\omega i}^T \mathbf{I}_i [\mathbf{r}_i \times] \mathbf{J}_{vi}]^T \right\} \end{aligned} \quad (23)$$

where,  $m_i, \mathbf{I}_i \in \mathbb{R}^3$  are  $i$ th link mass and inertia tensor,  $\mathbf{J}_{vi}, \mathbf{J}_{\omega i} \in \mathbb{R}^{3 \times n}$  stand for the Jacobian w.r.t. linear and angular velocity of each link,  $\mathbf{r}_i \in \mathbb{R}^3$  is the position vector of  $i$ th link CoM w.r.t. the base CoM. Here, we assume general  $n$ -link manipulator model. Note that base linear motion related terms are ignored for the sake of simplicity.

From (22), it can be seen that the manipulator producing kinetic energy is represented as a linear function in terms of the inertia parameters of manipulator. On the other hand, reaction wheel related energy is a quadratic function in terms of same parameters; it is also proportion to the inverse of the inertia moment of the reaction wheel. It should be noted that  $I_r$  is usually enough smaller than 1. Hence, it can be considered that the reaction wheel producing kinetic energy is far larger than the manipulator's one.

This feature makes reactionless motion potentially effective in terms of energy consumption because of no usage of reaction wheels. In addition, according to this feature, we can answer an other question: when these motions are not equivalent. As explained above, this error occurs at singularities of the coupling inertia matrix as shown in Fig. 17. This figures show that  $C_{err}$  projected on a plane (Fig. 17 (a)) and determinant of the coupling inertia matrix (Fig. 17 (b)). In Fig. 17 (a), dark area implies there is a large error. This area coincides the area where the determinant takes lowest value. With these configurations, reaction wheels are not needed because all motion induce zero reaction. As a result, reactionless motion does not coincide local minimum energy motion.

### 5.5. Comparison study in practical tasks

Here, we verify energy consumption of reactionless motion compared with reaction wheel based controller under the practical tasks as explained above.

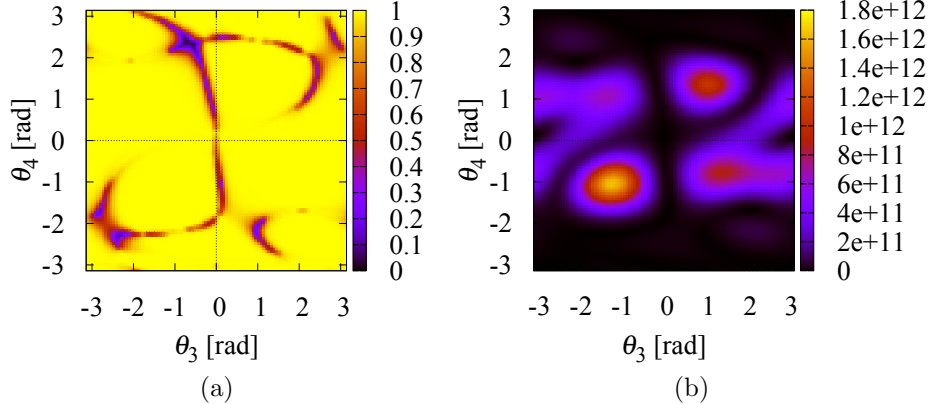


Figure 17: This figure shows that motion error occurs at singularities: (a)  $C_{err}$  projected on a plane and (b) determinant of the coupling inertia matrix.

### 5.5.1. Simulation condition

We consider the following cost functions:

$$T_{sum} = \frac{1}{2} \int_{t_0}^{t_f} \dot{\theta}^T(t) \Lambda \dot{\theta}(t) dt \quad (24)$$

$$T_{max} = \frac{1}{2} \max_{t_0 \leq t \leq t_f} (\dot{\theta}^T(t) \Lambda \dot{\theta}(t)) \quad (25)$$

(24) expresses whole kinetic energy, (25) is the maximum kinetic energy throughout the motion tasks.

In order to realize zero base-attitude deviation, the reaction wheel torque must be ensured the following condition:

$$\tau_r^{ref} = -\frac{d}{dt}(\tilde{M}_{\omega m} \dot{\theta}^{ref}(t)) \quad (26)$$

where,  $\dot{\theta}^{ref}$  is the pre-defined reference control command for the manipulator. Note that restriction of the output torque is not considered for the sake of simplicity, here.

We compare the above cost under the inspection and the PTP positioning maneuver with some initial configurations and the desired motions. In the inspection, simulation time is set as 20 s and the comparison controller is the inverse Jacobian controller using only the wrist assembly as explained the previous section.

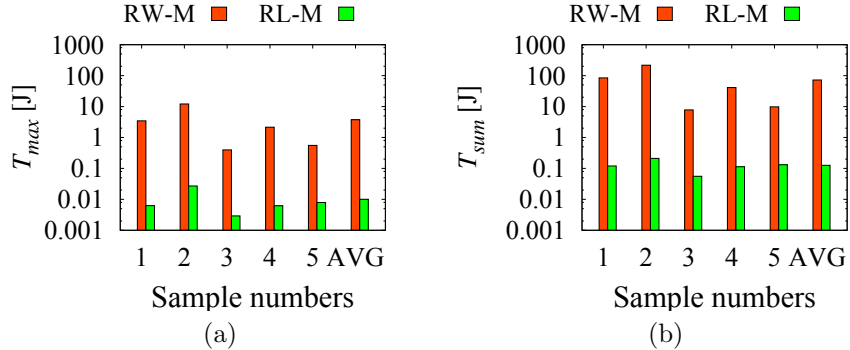


Figure 18: Energy consumption in inspection maneuver: (a) maximum kinetic energy and (b) integral of kinetic energy.

In the PTP maneuver, the positioning tasks were executed in 100 s duration. Also joint space interpolation with reaction wheel compensation was performed for comparison. In both maneuvers, simulations are executed in 5 conditions.

### 5.5.2. Simulation results

At first, the result in the inspection is displayed in Fig. 18. The red bar expresses the result with the reaction wheel based method, the green bar is that under the reactionless motion tasks. Note that  $y$  axis of the graphs is represented as log scale. From the results, it can be seen that energy consumption under reactionless motion is quite smaller than that of the reaction wheel based method. Actually,  $10^3$  times reduction is observed in the both cost functions. This results is due to the large energy consumption of reaction wheel as explained in (23).

In contrast to this, it can be seen that there is different results in the PTP maneuver. Reactionless motion can reduce energy consumption, but the amount of reduction is smaller than that in the inspection, because this motion maneuver has to use reaction wheels in Phase II. Nevertheless, energy consumption can be reduced almost 40% by using reactionless motion partially. From these results, it is confirmed that energy consumption of reaction wheel is quite larger than that of manipulator as explained in (23), analytically.

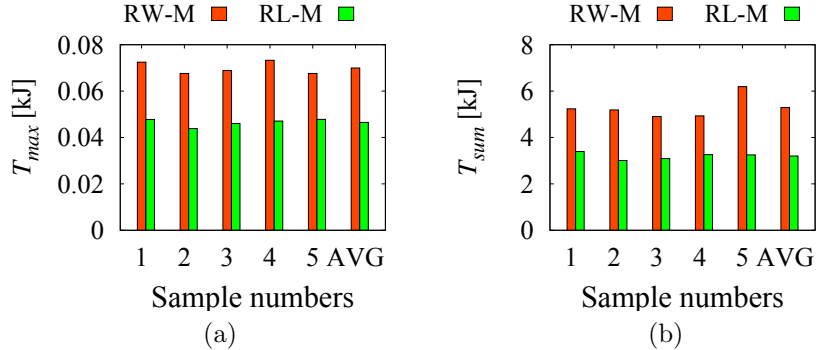


Figure 19: Energy consumption in the ptp positioning task: (a) maximum kinetic energy and (b) integral of kinetic energy.

## 6. Conclusion

In this work, we tackled two issues of reactionless motion control: (i) how to apply reactionless motion in practice and (ii) energy consumption of reactionless motion. In practical use, we have shown that for the specific seven-DoF redundant manipulator, which is quite common, reactionless motion can be obtained as a folding/unfolding motion via the elbow joint, and as a predominant wrist motion. Using these motions, we suggested three reactionless maneuvers as follows: (i) inspection maneuver using the end-effector hand camera, (ii) point-to-point motion maneuver with partial reactionless motion and (iii) extension maneuver from the stowed configuration. From the verification via numerical simulations, it was clarified that these maneuvers can be useful compared with the conventional control methods, such as joint space interpolation, inverse Jacobian and transpose Jacobian controller.

On the other hand, energy consumption of reactionless motion is still uncertainty compared with reaction wheel based approach. In this work, we show that reactionless motion almost coincides the local minimum energy motion under the zero base-deviation condition through numerical analysis. This feature is obtained through much higher energy consumption of reaction wheels than that of manipulator. Besides, we evaluated the benefit in terms of energy consumption when reactionless motion is used in the practical tasks. As a results, reactionless motion can reduce energy consumption compared with reaction wheel based control methods. For instance, energy consumption under reactionless control is  $10^3$  times smaller than that of reaction wheel based control in the inspection maneuver.

In summary, we can conclude that using reactionless motion provides two

advantages: (i) work efficiency through zero/small base-attitude deviation and (ii) energy consumption because of no usage of reaction wheel.

- [1] Y. Masutani, F. Miyazaki, S. Arimoto, Sensory feedback control for space manipulators, in: Proc. 1989 Int. Conf. Robot. Automat., 1989, pp. 1346–1351.
- [2] S. Dubowsky, M. Torres, Path planning for space manipulators to minimize spacecraft attitude disturbances, in: Proceedings. 1991 IEEE Int. Conf. on Robotics and Automation, 1991, pp. 2522–2528.
- [3] D. Nenchev, Y. Umetani, K. Yoshida, Analysis of a redundant free-flying spacecraft/manipulator system, *IEEE Trans. Robot. Autom.* 8 (1) (1992) 1–6.
- [4] D. N. Nenchev, K. Yoshida, Singularity-consistent teleoperation techniques for redundant free-flying robots, in: AIAA Guidance, Navigation, and Control Conference,, 1999, pp. 1895–1902.
- [5] K. Yoshida, K. Hashizume, S. Abiko, Zero reaction maneuver: flight validation with ETS-VII space robot and extension to kinematically redundant arm, in: Proc. IEEE Int. Conf. Robot. Automat., 2001, pp. 441–446.
- [6] D. Dimitrov, K. Yoshida, Utilization of the bias momentum approach for capturing a tumbling satellite, in: Proc. IEEE/RSJ Int. Conf. on Intelligent Robots and Systems, 2004, pp. 3333–3338.
- [7] S. V. Shah, I. Sharf, A. Misra, Reactionless path planning strategies for capture of tumbling objects in space using a dual-arm robotic system, in: Prof. AIAA Guidance, Navigation, and Control Conference, Reston, Virginia, 2013.
- [8] K. Yoshida, D. N. Nenchev, Reactionless manipulations and proposal to ETS-VII on-board experiments, in: International Symposium on Artificial Intelligence, Robotics and Automation in Space, 1999, pp. 1–3.
- [9] a. Pisculli, L. Felicetti, P. Gasbarri, G. Palmerini, M. Sabatini, A reaction-null/Jacobian transpose control strategy with gravity gradient compensation for on-orbit space manipulators, *Aerospace Science and Technology* 38 (2014) 30–40.

- [10] Y. Nakamura, S. Ito, Lowering energy consumption of Space robot systems through kinetic energy conservation, in: Proceedings IEEE International Conference on Robotics and Automation, 1993, pp. 20–25.
- [11] S. V. Shah, A. Gattupalli, Energy Optimum Reactionless Path Planning for Capture of Tumbling Orbiting Objects using a Dual-Arm Robot, in: Proceedings of the 1st International and 16th National Conference on Machines and Mechanisms, 2013, pp. 16–21.
- [12] R. Lamariello, G. Hirzinger, Generating feasible trajectories for autonomous on-orbit grasping of spinning debris in a useful time, in: 2013 IEEE/RSJ International Conference on Intelligent Robots and Systems, 2013, pp. 5652–5659.
- [13] K. Yoshida, Engineering test satellite VII flight experiments for space robot dynamics and control: theories on laboratory test beds ten years ago, now in orbit, *The International Journal of Robotics Research* 22 (5) (2003) 321–335.
- [14] D. Nenchev, K. Yoshida, P. Vichitkulsawat, M. Uchiyama, Reaction null-space control of flexible structure mounted manipulator systems, *IEEE Trans. Robot. Autom.* 15 (6) (1999) 1011–1023.
- [15] M. Oda, K. Kibe, F. Yamagata, ETS-VII, space robot in-orbit experiment satellite, in: Proc. IEEE Int. Conf. Robot. Automat., Vol. 1, 1997, pp. 739–744.
- [16] S. Taki, Y. Handa, N. Hara, D. Nenchev, Simple timing generation along workspace paths for nonredundant robotic limbs, *Advanced Robotics* 27 (18) (2013) 1409–1420.
- [17] D. Nenchev, K. Yoshida, Y. Umetani, Analysis, design and control of free-flying space robots using fixed-attitude-restricted jacobian matrix, in: The Fifth International Symposium on Robotics Research, 1990, pp. 251–258.
- [18] K. Yoshida, D. Nenchev, P. Vichitkulsawat, H. Kobayashi, M. Uchiyama, Experiments on the PTP operations of a flexible structure mounted manipulator system, *Proc. of IEEE/RSJ Int. Conf. on Intelligent Robots and Systems.* 1 (1996) 246–251.

- [19] M. Torres, S. Dubowsky, Path-planning for elastically constrained space manipulator systems, in: Proceedings IEEE International Conference on Robotics and Automation, 1993, pp. 812–817.